

# Controlling the roughening of growing electrochemical interfaces using temperature gradients

Asghar Aryanfar<sup>1,\*</sup>, Ali Tayyar<sup>2</sup>, and William A. Goddard, III<sup>3</sup>

<sup>1</sup>*Boğaziçi University, Mechanical Engineering, Bebek, Istanbul, Turkey 34342*

<sup>2</sup>*American University of Beirut, Mechanical Engineering, Riad El Solh, Beirut, Lebanon 1107 2020*

<sup>3</sup>*California Institute of Technology, 1200 E California Blvd, Pasadena, California 91125, USA*



(Received 3 November 2024; accepted 2 January 2025; published 24 January 2025)

The excessive dendritic development during the electrochemical evolution of the microstructures in rechargeable batteries can ultimately cause a short circuit, thermal instability, or runaway, and loss of active material. We initially develop a computational framework to quantify the bias of the electrodeposition on the roughened interface favoring the convex zones. Subsequently, we impose a countering temperature effect to enhance the diffusion on the trailing concave zones. Consequently, we establish a stability criterion for controlling surface roughening where the visualized space of parameters establishes a relationship between the geometry of the interface, the physical properties of the electrolyte, and the charging conditions. The developed framework could be useful for controlling the propagation of the microstructures and the prevention of runaway, during prolonged cycles, particularly when the surface roughness gets pronounced in the later stage of cycle life.

DOI: [10.1103/PhysRevE.111.015505](https://doi.org/10.1103/PhysRevE.111.015505)

## I. INTRODUCTION

The increasing necessity for energy in past years has required the innovation of higher-energy density energy storage systems with enhanced performance [1]. Among many technological innovations, batteries have shown great potential as a clean source of electrical energy. More recently, lithium-ion batteries (LIBs) have been widely used in portable electronics, manufacturing, and the electric cars and scooters industry [2,3] as well as the green energy sector [4,5], which exceeds billions of units manufactured throughout the world [6].

In a more specific way, LIBs have been widely investigated due to lithium's extremely high theoretical specific capacity ( $3860 \text{ mAhg}^{-1}$ ), low density ( $0.59 \text{ gcm}^{-3}$ ), the lowest negative electrochemical potential ( $-3.04 \text{ V}$  vs the standard hydrogen electrode) [7], and design flexibility [8]. In this regard, the growth of dendrites, a treelike microstructure induced by the expansion of conductive filaments on the lithium electrode has been a critical issue since they grow with extreme porosity, leading to excessive reach and causing short circuits [9,10]. As well, it may detach from the thinner part of the branches during the dissolution (i.e., discharge), and create the so-called dead lithium [11], causing thermal instability [12,13] and capacity decay [14,15].

The precise process of dendritic growth remains not entirely grasped, yet it is generally recognized to be impacted by several factors such as current density [16–18], electrolyte composition [12,19,20], solid electrolyte interphase (SEI) [21,22], and surface defects (i.e., kinks) [23]. The physical characterizations comprise porosity [24], tortuosity [25], and MacMullin number [26], the geometry and microscale curvature [27,28], and the sand time effect on growth transition [29].

The larger scale consequence of dendritic development can be attributed to a roughened interface where the developed models for stabilizing such an electrodeposited surface could be categorized into two realms of continuum and atomistics. From a continuum perspective, a small enough wavelength of perturbations in overlimiting currents leads to stable growth [27], imposing prestress can increase the stability span of the undulations [30], using viscous electrolyte can level the growing interface via limiting the electroconvection [31,32], and simultaneous evolution of curved interface with the SEI can alter the interface geometry due to thickness dependent variation in the resistance of SEI, below its critical value [33]. As well, the artificial design of the strong solid-electrolyte interface can suppress the formation of roughened surfaces (i.e., dendrites) [34].

From an atomistic perspective, the convex electrode curvature (bent into the electrolyte) has shown a positive effect on stabilizing the growing morphology [28], curvature-induced local straining can favorably alter lithophilicity on an electrode surface [35], and formation of small lithium aqueous and nonaqueous electrolytes could provide additional electrode or electrolyte passivation and control [36]. As well, the fractal dimension of the microstructures has been shown to be curvature-independent [37]. Other works on the electrochemical interfaces include phase-field modeling [38–40], coarse-grained modeling in time [41], sharp interface modeling via an extending space-charge region, and considering nonlinear electrode reactions [42].

Several engineering ideas have tried to control the dendritic propagation, including shielding techniques [43], curvature-induced structural modification [44], imposing external magnetic fields [45], guiding scaffolds [46], using nanofiber arrays in the polymer electrolyte [47], applying prestress to stabilize planar growth and reduce surface roughening, [30], and using an-isotropic electrolytes to controlling electric-field gradients offering potential strategies to improve battery stability and

\*Contact author: [aryanfar@caltech.edu](mailto:aryanfar@caltech.edu)

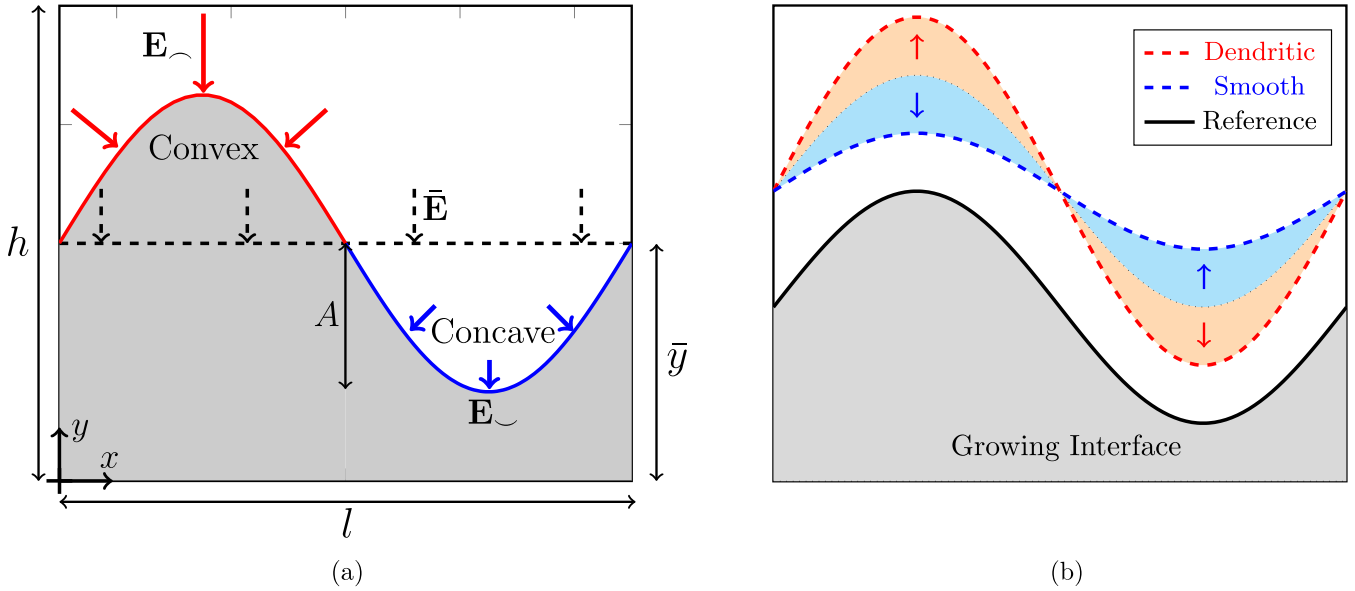


FIG. 1. The convex and concave regions in the perturbed interface are compared in terms of (a) electric field and (b) growth stability; (a) Surface heterogeneity model: Black dashed arrows illustrate the average electric field for the equivalent flat geometry.  $h$ ,  $l$ : domain height and length,  $\bar{y}$ : average elevation of interface,  $x$ ,  $y$ : coordinates. (b) The illustration of evolution dynamics, where the reference interface (i.e., black) can either grow stable (i.e., blue) or unstable (i.e., red). In stable growth, the convex (top) and concave (bottom) regions get closer to each other (blue arrows), while during unstable growth they get further away from each other (red arrows).

potentially suppressing dendrite formation [48]. Additionally, they have ascribed that the growth rate could be controlled when lowering the charge transfer coefficients [49], applying forced advection and cross flow [50,51]. The higher surface roughness and thinner SEI layer could exacerbate the dendritic propagation [52–54] and describe the kinetics of roughening interfaces via incorporating surface tension and elastic and viscous effects [55]. As well, for the engineered undulations, superfills have been used as an additive chemical to enable preferential metal deposition on the bottom regions and avoiding the formation of cavities [56], and their efficacy of correlates directly with the curvature of the undulations [57].

Another factor for the electrodeposition, which has long been studied in piezoelectric materials [58,59] and can alter the fate of the formed interface, is mechanical factors such as surface tension [60,61] and imposing external pressure and stress [62], as an additional term in the electrochemical potential [63,64].

In the meantime, the temperature is a key parameter, the effect of which has proven to be instrumental in the experimental surface film growth [65], as well as in the molecular dynamics simulations of  $\text{Li}^+$  diffusional transport in the SEI (i.e., 250–400K) [66]. More specifically, temperature has been explored to shape the surface morphology and dendrite formation of microstructures [67–69]. It has been shown that elevated temperatures (i.e.,  $60^\circ - 80^\circ$ ) transform the SEI layer into a uniform compact layer which can delay the instigation of dendrites [70,71]. However, later, lowering the system temperature increases the diffusion resistance and decreases the surface film thickness, which is favorable for suppressing the dendrites [72,73].

While the presence of surface roughness, consisting of the convex (i.e., peak) and concave (i.e., valley) regions, favors the electrodeposition in the convex zones, in this paper we

counter such effects via imposing a temperature field in the opposite direction, which forms a bias for favoring the electrodeposition in the concave (i.e., valleys) sites. Obtaining the voltage  $V$  and temperature field  $T$ , we characterize the space of physical parameters for the efficacy of the imposed temperature gradient. The obtained framework could be useful for controlling the growing dendrites in electrochemical systems, particularly those consuming larger power, where the microstructures could grow with runaway behavior.

## II. METHODOLOGY

From the atomic perspective, dendritic propagation and formation of rough interfaces are inevitable, and fast processes occur under nonequilibrium conditions. Such a kinetics-dominated event rapidly accumulates the ions with random walks (i.e., Brownian dynamics), which is distinguishable from typical thermodynamics-dominated bonding under slow, close-to-equilibrium conditions.

From the continuum perspective, the development of the interfacial morphology depends on the macroscale electrochemical parameters which include the electric field and electrolyte diffusivity. Such variables control the accessibility of ions to the electrodeposition sites and the rate of interface growth.

As shown in Fig. 1(a), such stochastic interactions should yield a fast-growing asperity (i.e., convex:  $\frown$ ), followed by a slow-growing hollow region (i.e., concave:  $\smile$ ). The difference in the growth rate is due to the peaks having better proximity for the upcoming ions as well as possessing geometry-induced higher directed electric field ( $E_{\frown} > E_{\smile}$ ). Hence, the evolved microstructures will acquire a certain roughness, which grows with runaway behavior [29,74]. Therefore, we aim to counter such instability by imposing a reaction-rate bias in favor of

the concave region, which is controlled by the temperature field  $T$ .

### A. Electric field

The perturbation in the growing interface can be modeled in a sinusoidal form, where concave (i.e., valley:  $\cup$ ) and convex (i.e., peak:  $\cap$ ) regions are connected as shown in Fig. 1(b). The elevation of the interfacial roughness  $y_I$  could be expressed in terms of the horizontal variable  $x$  as

$$y_I = \bar{y} + A \sin\left(\frac{2\pi\omega x}{l}\right), \quad (1)$$

where  $\bar{y}$  is the average elevation of the growing microstructure,  $A$  is the amplitude of the perturbation,  $\omega$  is the frequency of the repetition, and  $l$  is the domain length. Thus, the maximum curvature  $\kappa$  occurs in the peaks and valleys ( $|\sin(\dots)| = 1 \rightarrow x = \pm l/4\omega$ ) as

$$\kappa = \frac{y_I''}{\sqrt{(1 + y_I'^2)^3}} \Big|_{x=\frac{l}{4\omega}} = -A \left(\frac{2\pi\omega}{l}\right)^2. \quad (2)$$

Therefore, one can calculate the ratio of the maximum-to-minimum electric field  $\hat{E} := E_{\cap}/E_{\cup}$ , which is a measure of how critically the roughening interface. In this regard, the maximum and minimum electric field depend on both the radius of curvature  $r$  (i.e.,  $r = 1/\kappa$ ), the applied voltage of  $V_+$  and  $V_-$  between two electrodes as well as the remaining distance of the interface from the counter electrode (i.e.,  $h - y_I$ ). Thus, the electric field in any position can be described as

$$E = f(r) \frac{V_+ - V_-}{h - y_I}, \quad (3)$$

where  $f(r)$  is the curvature dependents augmentation (or diminishing) factor based on the interface geometry. Particularly, the ratio of the electric field  $\hat{E}$  between the convex  $E_{\cap}$  and concave  $E_{\cup}$  surfaces (i.e.,  $\hat{E} = E_{\cap}/E_{\cup}$ ) is obtained as

$$\hat{E} = \frac{f_{\max}(\hat{r})}{f_{\min}(\hat{r})} \frac{h - y_{\min}}{h - y_{\max}},$$

where  $y_{\min}$  and  $y_{\max}$  are the respective elevations at concave and convex surfaces and  $\hat{r} := r/h$  is the normalized radius of curvature. In fact, for the convex interface, the electric field is augmented [ $f_{\max}(\hat{r}) > 1$ ], and vice versa for the concave interface it gets diminished [ $f_{\min}(\hat{r}) < 1$ ]. Hence, in terms of the curvature effect, one gets the following order:

$$E_{\cap} > \bar{E} > E_{\cup}, \quad (4)$$

where the indexes  $\cap$ ,  $\bar{\cap}$ , and  $\cup$  represent the convex (i.e., peak), flat, and concave (i.e., valley) regions, respectively.

### B. Temperature gradient

The temperature has a deterministic role in the rate of the electrodepositing reactions, which is generally expressed via the Arrhenius relationship. The diffusivity of the ions  $D$  within the electrolyte is governed by the following relationship [75]:

$$D = D_0 \exp\left(-\frac{Q}{k_B T}\right), \quad (5)$$

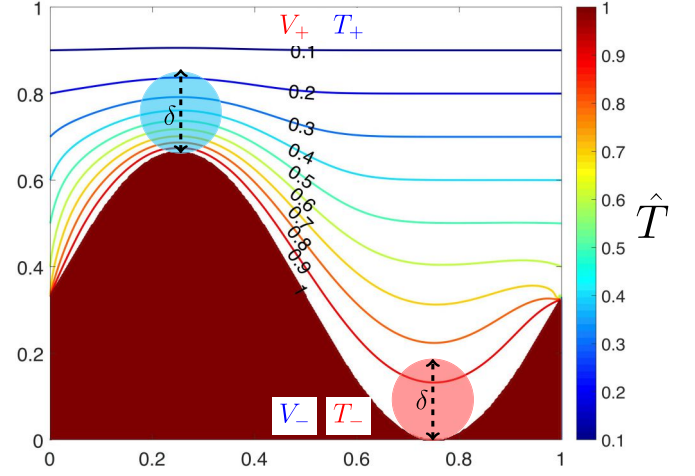


FIG. 2. The temperature map for the roughened surface is characterized by convex (*peaks*) and concave (*valleys*) regions. Lines show the dimension-less temperature map [i.e.,  $\hat{T} = (T - T_+)/(T_- - T_+)$ ], with the bottom (i.e.,  $T_-$ ) and top (i.e.,  $T_+$ ) electrode temperatures. The growing interface remains isothermal with the connected electrode (i.e.,  $T_-$ ). The temperature distribution is obtained later in Sec. III.

where  $D_0$  is a prefactor and  $Q$  is the activation energy for the diffusivity, and  $k_B$  is the Boltzmann's constant. Figure 2 illustrates a sample of a formed temperature field in the vicinity of the convex (blue circle) and concave (red) sites when a higher temperature is imposed in the negative electrode ( $T_- > T_+$ ). Since the concave region is surrounded by a higher temperature interface, it will get a higher temperature. Conversely, the sticking-out convex peak will have less of the higher temperature interface in its surroundings and hence gets lower temperature values. Consequently, the concave regions possess warmer electrolytes than their convex counterpart. In this context, while the electric field forms a bias for more growth in the convex region, imposing the higher temperature at the negative electrode could cause a countering bias for more electrodeposition in the concave sites. This could be explained in terms of the ionic flux  $J$ , which is described as [76]:<sup>1</sup>

$$J = -D\nabla C - \frac{zF}{RT} DC\nabla V \quad (6)$$

where  $D$  is the diffusivity of the ions in the electrolytic medium,  $C$  is the local concentration of the electrolyte,  $z$  is the valence number of the charge carriers,  $F$  is the Faraday's constant,  $R$  is the gas constant,  $T$  is the local temperature, and  $V$  is the local voltage. Therefore, while the electric field  $E$ , as a nonmaterial-independent property, favors higher flux in the convex interface, the diffusivity as a material-dependent property could favor higher ionic flux at the concave sites and balance out the electrodeposition for forming more uniform interface, and one gets

$$D_{\cup} > \bar{D} > D_{\cap}, \quad (7)$$

which tends to counter the the electric field effect obtained earlier in Eq. (4).

<sup>1</sup>In the absence of convection.

TABLE I. Physical parameters.

Variable	$D$	$C_0$	$l$	$R$	$T$	$V_0$	$z$	$F$
Value	$2.3 \times 10^{-10}$	$10^3$	25	8.3	298	3.6	1	96.4
Unit	$\text{m}^2 \text{s}^{-1}$	$\text{mol m}^{-3}$	$\mu\text{m}$	$\text{J mol}^{-1} \text{K}^{-1}$	$K$	$V$	[ ]	$kC \text{mol}^{-1}$
Ref.	[77]	Assumed	[78]	[79]	Ambient	[80]	for $\text{Li}^+$ [81]	[79]

### C. Stability condition

The comparative scale of the convex and concave zones, illustrated in Fig. 2, falls in the continuum realms, which extends significantly larger than the smaller-scale electrodeposition sites in the interface (i.e., Helmholtz layer, double

layer, space-charge, etc.). Such a large-scale zone is in the electroneutral condition [82], where the continuum relationship for ionic flux is in effect. In fact, the ionic flux [Eq. (6)] is composed of mainly diffusion ( $D\nabla C$ ) and electromigration [ $(zF/RT)DC\nabla V$ ]. Herein, we compare these two terms using the typical value in Table I, as below:

$$J_{\text{diff}} = D\nabla C \sim \frac{2DC_0}{l} \sim 10^{-2} \frac{\text{mol}}{\text{m}^2 \text{s}} \quad \text{diffusion}$$

$$J_{\text{mig}} = \frac{zF}{RT} DC\nabla V \sim \frac{De}{k_B T} zFC_0 \frac{V_0}{l} \sim 1 \frac{\text{mol}}{\text{m}^2 \text{s}} \quad \text{electromigration,}$$

which means that for the typical value  $J_m \gg J_{\text{diff}}$ ; not to mention that for the voltage  $V$ , the effective zone of variation is the space-charge region (i.e.,  $x_f$ ) [82], which would make  $J_{\text{mig}}$  even larger. In fact, the migration efficacy for ionic flux occurs when the applied voltage is high enough. In such conditions, the drift velocity  $v_d$  of the charge carriers will be effective, which feeds the electrodeposition sites and determines the rate of interface growth, and is defined as [81]

$$v_d = \mu \mathbf{E}, \quad (8)$$

where  $\mu$  and  $\mathbf{E}$  are the local ionic mobility and electric field, respectively. As well, considering the correlation of the electrical mobility  $\mu$  with the diffusivity  $D$  (i.e., Einstein relationship where  $\mu \sim D/T$ ), one would require faster electrodeposition in the concave zone and the convex counterpart for achieving stability (i.e.,  $v_{d,\sim} > v_{d,\cap}$ ). Hence, assuming similar grown porosity in the convex and concave zones, one gets

$$\frac{D_{\sim} E_{\sim}}{T_{\sim}} > \frac{D_{\cap} E_{\cap}}{T_{\cap}}, \quad (9)$$

where considering the correlation of the diffusivity  $D$  with the temperature  $T$  [Eq. (5)], one achieves

$$\frac{T_{\sim}}{T_{\cap}} \exp\left(\frac{Q}{k_B} \left(\frac{1}{T_{\sim}} - \frac{1}{T_{\cap}}\right)\right) > \frac{E_{\sim}}{E_{\cap}}, \quad (10)$$

and the required activation energy of the electrolyte  $Q$ , such that the concave zone ( $\sim$ ) could catch up with the convex zone ( $\cap$ ), is obtained as

$$Q > \frac{T_{\sim} T_{\cap}}{T_{\sim} - T_{\cap}} k_B \ln\left(\frac{E_{\sim} T_{\sim}}{E_{\cap} T_{\cap}}\right), \quad (11)$$

which provides the stability criterion for the stable evolution of the interfacial perturbation when the temperature gradient is imposed.

## III. NUMERICAL COMPUTATION

### A. Voltage distribution $V$

To calculate the maximum  $E_{\sim}$  and minimum  $E_{\cap}$  electric fields, one needs to compute the voltage distribution in the vicinity of these sites. In this regard, Poisson's equation could describe the continuum voltage mapping, given as [83]

$$\nabla^2 V = \frac{\rho}{\epsilon}, \quad (12)$$

where  $\rho$  is the local charge density and  $\epsilon$  is the permittivity of the electrolyte medium. Due to the large scale of the interface perturbation ( $\sim \mu\text{m}$ ), a fair assumption is that a significant portion of the medium falls out of the double layer region ( $\sim \text{nm}$ ). Therefore, a simplified version of Eq. (12) for the voltage distribution in 2D would be [84]

$$\frac{\partial^2 V}{\partial x^2} + \frac{\partial^2 V}{\partial y^2} \approx 0. \quad (13)$$

Therefore, the domain could get partitioned into a 2D grid of  $n_x \times n_y$  points where  $n_x$  and  $n_y$  are the number of grid points in  $x$  and  $y$  directions, respectively, which are selected large enough to be able to capture the voltage variations in the convex ( $\cap$ ) and concave ( $\sim$ ) sites.

Hence,  $V_{i,j}$  represents the voltage at nodes  $x_j$  and  $y_i$ . Performing a finite difference scheme on Eq. 13, one has

$$\frac{(V_{i,j+1} - 2V_{i,j} + V_{i,j-1}))}{\delta x^2} + \frac{(V_{i+1,j} - 2V_{i,j} + V_{i-1,j}))}{\delta y^2} \approx 0. \quad (14)$$

Rearrangement gives

$$V_{i,j} \approx \frac{V_{i+1,j} + V_{i-1,j} + \frac{\delta y^2}{\delta x^2} (V_{i,j+1} + V_{i,j-1}))}{2(1 + \frac{\delta y^2}{\delta x^2})}. \quad (15)$$

Regarding the boundary conditions, from Fig. 1(a), since the metallic interface is physically connected to the negative



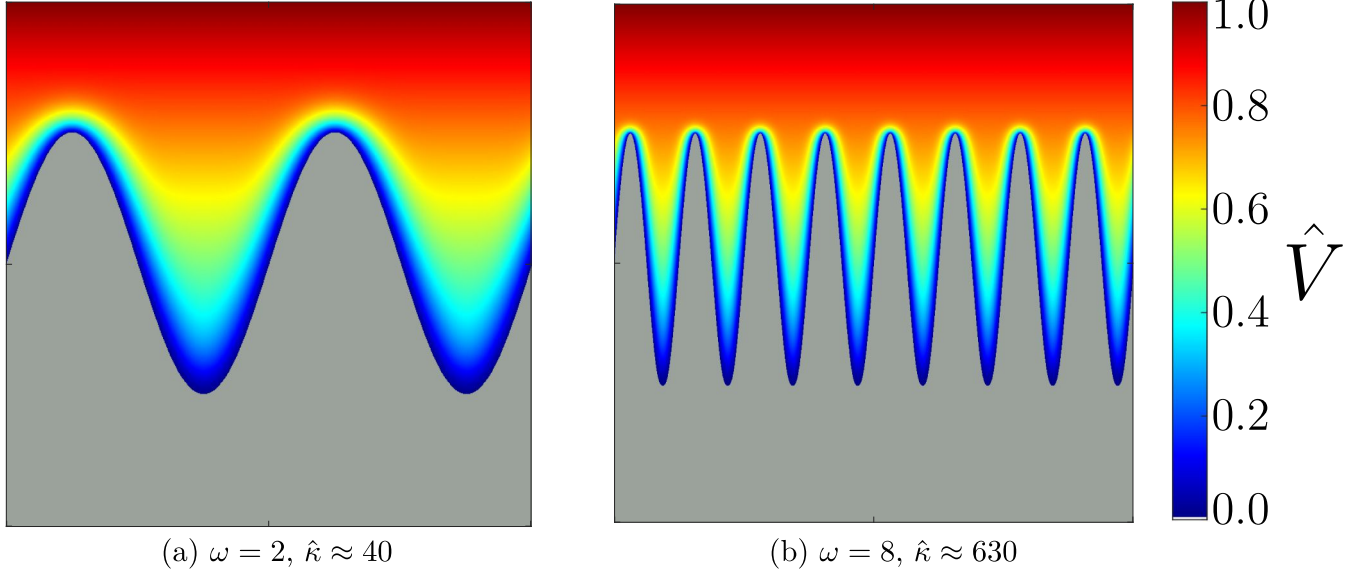


FIG. 3. The distribution in the normalized voltage  $\hat{V}$  for various normalized curvatures  $\hat{\kappa}$ . Gray area represents the growing (i.e., dendritic) interface.

pole, one has

$$\begin{aligned} V(x, 0) &= V_- & y &= 0 \\ V &= V_- & y &\leq y_I \\ V(x, h) &= V_+ & y &= h, \end{aligned} \quad (16)$$

which are the Dirichlet boundary conditions for the discretized Eq. (15), and  $V_-$  and  $V_+$  are the voltage values for the negative electrode and positive electrode.

The initial voltage value  $V_0$  is set as the uniform distribution in the domain between the negative and positive electrode, except the interface which is physically touching the negative electrode ( $V_-$ ) as

$$V_0(x, y) = \begin{cases} V_- & y \leq y_I \\ V_- + \left(\frac{V_+ - V_-}{h}\right)y & y > y_I. \end{cases} \quad (17)$$

Subsequently, the voltage of the grid points  $V_{i,j}$  was updated from the neighboring grid points (top  $\uparrow$ , bottom  $\downarrow$ , left  $\leftarrow$ , and right  $\rightarrow$ ), through the successive steps based on Eq. (15). During each iteration, the boundary conditions, in Eq. (16) were enforced from the electrodes and the interfaces. As well, regarding the left and right boundaries, the periodic boundary condition (PBC) was applied, which indicates that the voltage values between the left and right boundaries are transferred to each other.

Throughout the successive runs, the convergence criterion is defined by a maximum difference of the voltage values  $V_{i,j}$  varying of next iteration ( $k+1$ ) from the previous one ( $k$ ), which is tracked as the error. The iterations were stopped when the error value got smaller (or equal) to the assigned threshold value. Figure 3 visualizes the converged final voltage distribution for both low- (i.e., small  $\omega$ ) and high-curvature (i.e., large  $\omega$ ) perturbations [85].

Finally, the average electric field across the highlighted regions of the convex (i.e.,  $E_-$ ) and concave (i.e.,  $E_+$ ) regions in Fig. 2 are calculated via approximating  $E = -\nabla V$  as

$$E \approx \frac{V_{\text{top}} - V_{\text{bot}}}{\delta}, \quad (18)$$

where  $V_{\text{top}}$  and  $V_{\text{bot}}$  are the converged voltage values in the top and bottom ends of the focused zones in both convex ( $\cap$ ) and concave ( $\cup$ ) zones and  $\delta$  is their respective diameter.

## B. Temperature distribution $T$

The relationship for transition and dispersal of the temperature is expressed as [86]

$$\frac{\partial T}{\partial t} = \alpha \left( \frac{\partial^2 T}{\partial x^2} + \frac{\partial^2 T}{\partial y^2} \right), \quad (19)$$

since the rate of growth in the moving boundary  $\partial y_I / \partial t$  is far less than the dynamics of the convergence of the temperature  $(\partial T / \partial t) [(\partial y_I / \partial t) \ll (\partial T / \partial t)]$ ; during the growth process, the boundary could get assumed as quasistationary with respect to the transition of the temperature field, which means that the temperature profile can be treated as the quasisteady state  $\partial T / \partial t \approx 0$ , and the temperature profile is given via

$$\frac{\partial^2 T}{\partial x^2} + \frac{\partial^2 T}{\partial y^2} \approx 0 \quad (20)$$

regarding the boundary conditions; the temperature values are constant in the electrodes after applying the temperature gradient ( $T_- > T_+$ ). As well, since the thermal diffusivity of the growing metallic interface  $\alpha_I$  is significantly larger than the nonmetallic metallic boundary  $\alpha_{EI}$  ( $\alpha_I \gg \alpha_{EI}$ ), the rate of temperature variation will also be significantly larger and it remains relatively isothermal with the electrode (i.e.,  $T_-$ ). This means that the interface temperature could be assumed as the quasisteady state compared to the electrolytic domain, and the

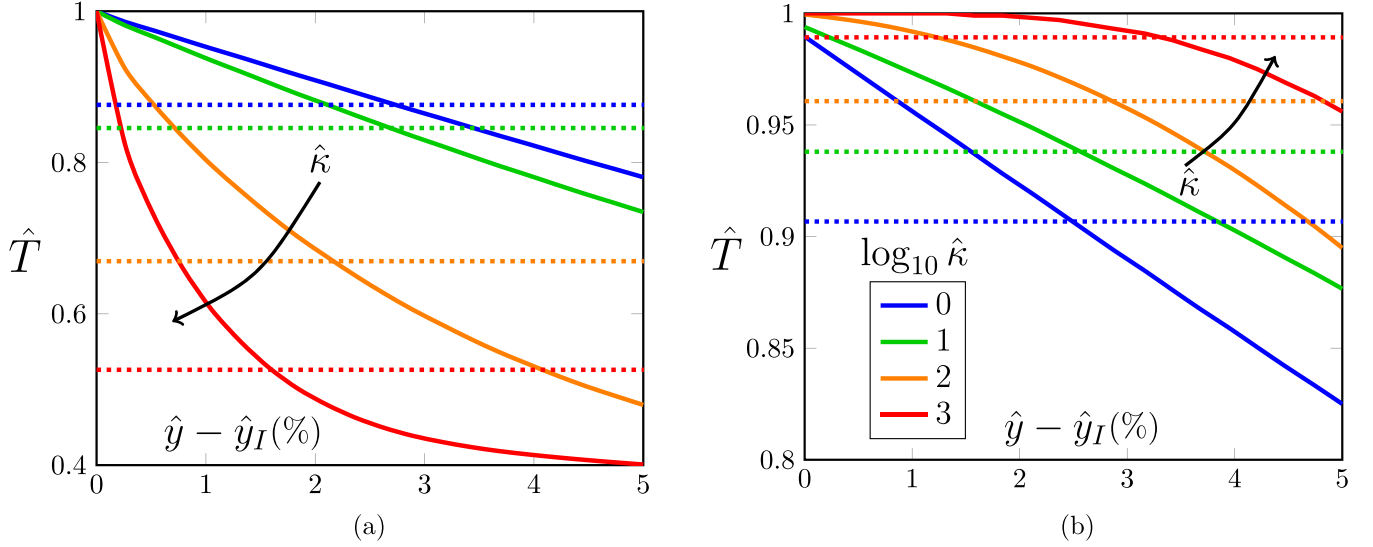


FIG. 4. The normalized temperature profile  $\hat{T}$  versus the normalized vertical distance  $\hat{y} - \hat{y}_I$ , above (a) the convex (i.e., peak) and (b) the concave (i.e., valley) regions for various normalized curvature values  $\hat{\kappa}$ .

temperature boundary condition will be established as

$$\begin{aligned} T(x, 0) &= T_- \\ T &= T_- \quad y \leq y_I \\ T(x, h) &= T_+. \end{aligned} \quad (21)$$

It is noticeable that the relationships and boundary conditions for the temperature in Eqs. (20) and (21) are similar to the relationships for the voltage distribution in Eqs. (13) and (16). Hence, one can avoid repeated computations by projecting the temperature profile  $T$  from the voltage profile  $V$ . In this regard, we define the dimensionless parameters for the voltage  $\hat{V}$  and temperature  $\hat{T}$  as

$$\begin{aligned} \hat{V} &= \frac{V - V_-}{V_+ - V_-} \quad 0 \leq \hat{V} \leq 1 \\ \hat{T} &= \frac{T - T_+}{T_- - T_+} \quad 0 \leq \hat{T} \leq 1. \end{aligned}$$

Noting that the gradient of the temperature field is imposed as opposite to the voltage field, the temperature field is obtained as

$$\hat{T} = 1 - \hat{V}. \quad (22)$$

Figures 4(a) and 4(b) illustrate the variation of the temperature versus the normalized vertical distance above the convex (i.e., peak) and concave (i.e., valley) sites ( $\hat{y} - \hat{y}_I$ ), respectively. Here, one can infer the effect of the curved boundary on the temperature profile as

$$\left. \frac{\partial^2 T}{\partial \hat{y}^2} \right|_{\curvearrowright} < 0, \quad \left. \frac{\partial^2 T}{\partial \hat{y}^2} \right|_{\curvearrowleft} > 0,$$

which means that the average temperature in the convex  $\bar{T}_{\curvearrowright}$  and concave  $\bar{T}_{\curvearrowleft}$  sites (blue and red circles in Fig. 2) differ considerably, which can be obtained via integrating in the

region as

$$\bar{T} = \frac{1}{\delta} \int_0^\delta T dy,$$

and one gets

$$\bar{T}_{\curvearrowright} > \bar{T}_{\curvearrowleft}, \quad (23)$$

which are shown as dashed lines in these two figures.

## IV. RESULTS AND DISCUSSIONS

### A. Stability analysis

The temperature difference, given in Eq. (23), provides the possibility for higher diffusion of the ions in the concave ( $\curvearrowleft$ ) sites relative to the convex ( $\curvearrowright$ ) counterpart regions. One effective parameter for the imposed temperature gradient  $\Delta T$  is the sensitivity of the resulted diffusivity  $D$ , which can be obtained as

$$\frac{\partial D}{\partial T} = -\frac{Q}{k_B T} D.$$

Here it is evident that one effective parameter for such sensitivity is the activation energy  $Q$ . In other words, for an electrolyte more responsive to the temperature (i.e.,  $Q \uparrow$ ), less temperature is needed ( $\Delta T \downarrow$ ) to form stable growth. Considering the halfway progress of the interface ( $\bar{y} = h/2$ ), Figures 5(a)–5(c) visualize the range of required temperature gradient  $\Delta T$  versus the diffusion activation energy  $Q$  of the electrolyte for three quartiles of destabilization  $\hat{A} = \{1/4, 1/2, 3/4\}h/2$ , which is additionally characterized in terms of interface curvature  $\hat{\kappa} = \kappa/h$  [85].

In this regard, the earlier slower growth of the stable zone (i.e.,  $\hat{A} = \{1/4 \rightarrow 1/2\}h/2$ ) and its later fast diminishing (i.e.,  $\hat{A} = \{1/2 \rightarrow 3/4\}h/2$ ) could be explained via the nonlinear overall effect of the electric field  $E$  versus the temperature field  $T$  [Eq. (10)]. Labeling the temperature and electric field roles as  $f_T := T_-/T_+ \exp(Q/k_B(1/T_- - 1/T_+))$  and  $f_E := E_-/E_+$ , respectively, the stable growth could get obtained when  $f_T > f_E$ . Therefore, during the earlier transition from

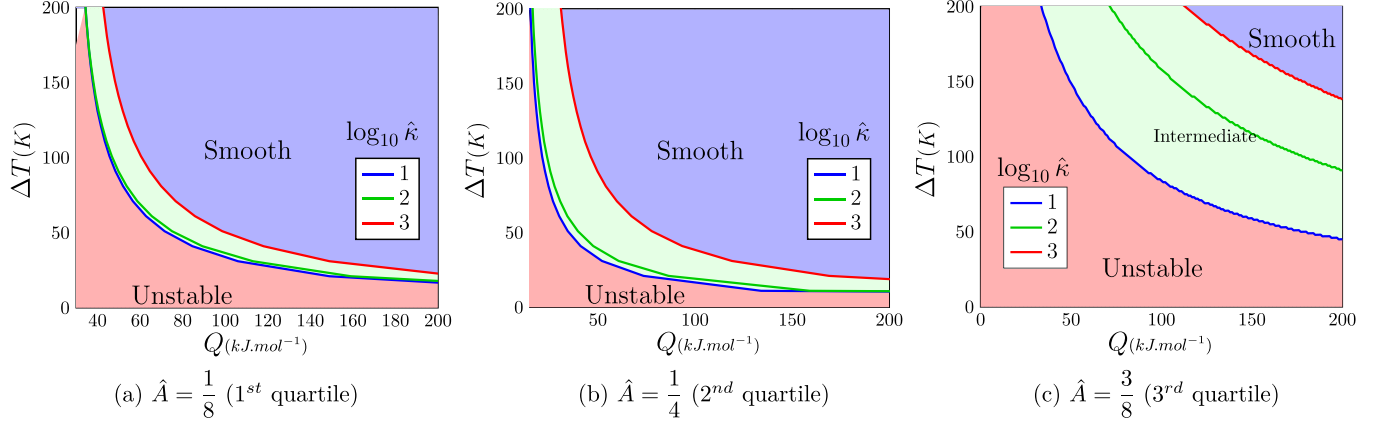


FIG. 5. Visualized zones of the required temperature difference  $\Delta T$  versus the activation energy  $Q$ , for halfway progress of the interface (i.e.,  $\bar{y} = h/2$ ) for three-quarters of the destabilized growth ( $\hat{A} = \{1/4, 1/2, 3/4\}$ ). The stable zones (blue) signify diffusion domination, and vice versa, the unstable zones (red) illustrate electromigration domination.

the first to second quartile, it is obvious from Eq. (11) that while the competitive ratios of  $E_-/E_+$  and  $T_-/T_+$  carry smaller weight in the logarithm term, the primary impact is derived from the temperature difference as

$$Q > \sim \frac{1}{T_- - T_+}.$$

In this regard, since the dimensionless voltage  $\hat{V}$  and temperature  $\hat{T}$  fields have been found to be complementary of each other in Eq. (22), one could ascribe the following correlation:

$$\hat{T} = 1 - \int_0^\delta \hat{E} dy,$$

which means that the temperature field would be averaging the values across the focus region of scale  $\delta$  (Fig. 2). In this regard, while considering solely the temperature ratio  $T_-/T_+$  between the concave and convex sites would carry a smaller effect than the electric field ratio  $\hat{E}$ , the exponential term  $\exp(Q/k_B(1/T_- - 1/T_+))$  empowers overall temperature effect  $f_T$ , which makes it ultimately dominate.

However, during the later transition from the second to third quartile, since the difference in the remaining gap between the convex and concave sites grows rapidly, the overall electric field effect accelerates further and the required temperature gradient needs to be much higher. Such a destabilizing trend is additionally observed versus the curvature increase in all these figures.

### B. Curvature effect formulation

While the role of the curvature  $f(\hat{r})$  has been qualitatively explored in the previous sections, such an augmentation (diminishing) coefficient for convex (concave) zones could get addressed quantitatively. In this regard, Eq. (3) can get normalized as

$$\hat{E} = \frac{f(\hat{r})}{1 - \hat{y}_I},$$

where  $\hat{y}_I = y_I/h$  is the normalized average interface elevation. Considering a single semicircle with the prescribed normal-

ized radius of curvature  $\hat{r} = r/h$ , set in the center of the domain, one could recalculate the voltage field, repeating the procedure in Sec. III. Figures 6(a) and 6(b) illustrate the resulting voltage distributions for a convex and concave interface, respectively.

From Fig. 6(a), the augmentation coefficient  $f_{\max}$  of the electric field in the convex sites due to the radius of curvature could be formulated. As an initial step, the limits can be placed, where for the minimal radius of curvature this radius gets indefinitely large, and vice versa for the very large radius of curvature it becomes ineffective. Hence,

$$\lim_{\hat{r} \rightarrow 0} f_{\max} = \infty$$

$$\lim_{\hat{r} \rightarrow \infty} f_{\max} = 1.$$

Therefore, one could assign an interpolating function satisfying these boundary conditions, as below:

$$f_{\max} = \frac{\exp(\alpha_1 \hat{r}) + \beta_1}{\exp(\alpha_1 \hat{r}) - 1}, \quad (24)$$

where  $\alpha_1$  and  $\beta_1$  are the relaxation coefficients. Similarly, for Fig. 6(b), the diminishing coefficient  $f_{\min}$  of the electric field in the concave regions due to the radius of curvature could be interpolated. In this regard, for the minimal radius of curvature, this coefficient gets indefinitely small, and vice versa for a very large radius of curvature it yields to unity (i.e., becomes ineffective). Hence,

$$\lim_{\hat{r} \rightarrow 0} f_{\min} = 0$$

$$\lim_{\hat{r} \rightarrow \infty} f_{\min} = 1,$$

and one can define an interpolating function form to satisfy the above boundary condition as

$$f_{\min} = \frac{\exp(\alpha_2 \hat{r}) - 1}{\exp(\alpha_2 \hat{r}) + \beta_2}, \quad (25)$$

where  $\alpha_2$  and  $\beta_2$  are the relaxation coefficients. For either augmentation or diminishing ratios, the coefficients of  $\alpha_i$  and

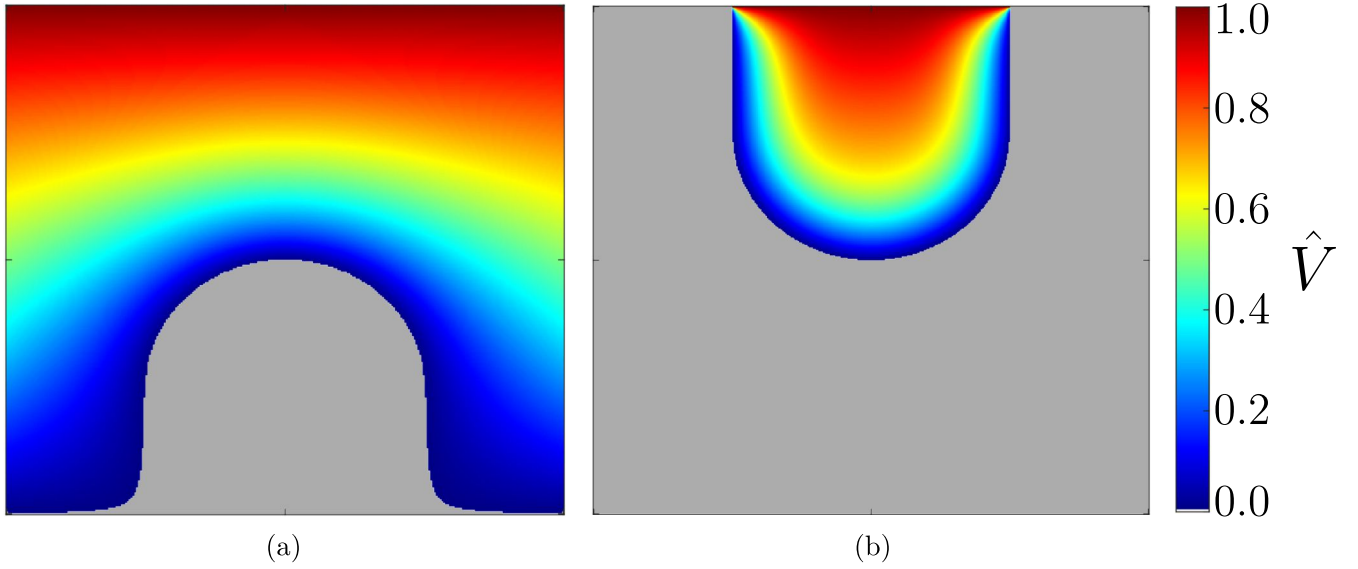


FIG. 6. Voltage distribution on the vicinity of a single (a) peak and (b) valley-prescribed radius of curvature (i.e.,  $\hat{r} = 1/\kappa$ ), set in the center of the domain ( $y_I = h/2$ ). The grey region represents the grown interface (i.e.,  $V = V_-$ ). (a) Normalized voltage map surrounding a convex region of the prescribed radius of curvature  $\hat{r} = 1/4$ , which augments the electric field on its high peak and is addressed by  $f_{\max}$ . (b) Normalized voltage map surrounding a concave region of the prescribed radius of curvature  $\hat{r} = 1/4$ , which diminishes the electric field on its bottom valley and is addressed by  $f_{\min}$ .

$\beta_i$  are obtained via minimizing the sum of the squares of the errors from the computational values  $\hat{E}$  in the locus of  $y_{\max}$  and  $y_{\min}$  as

$$\forall \alpha_i, \beta_i \in \mathbb{R} \quad \text{minimize Err} \\ \text{Such that} \quad \text{Err} = \sum_{k=1}^n \left| \frac{f_k}{1 - \hat{\lambda}_k} - \hat{E}_k \right|^2,$$

where  $n$  is the number of points from the numerical computations.<sup>2</sup> Figures 7(a) and 7(b) illustrate the nonlinear behavior in the augmentation and diminishing factors ( $f_{\max}$ ,  $f_{\min}$ ) versus the normalized radius of curvature  $\hat{r}$  for

<sup>2</sup>Also obtainable using nonlinear fitting function in MATLAB (i.e., `nlinfit`).

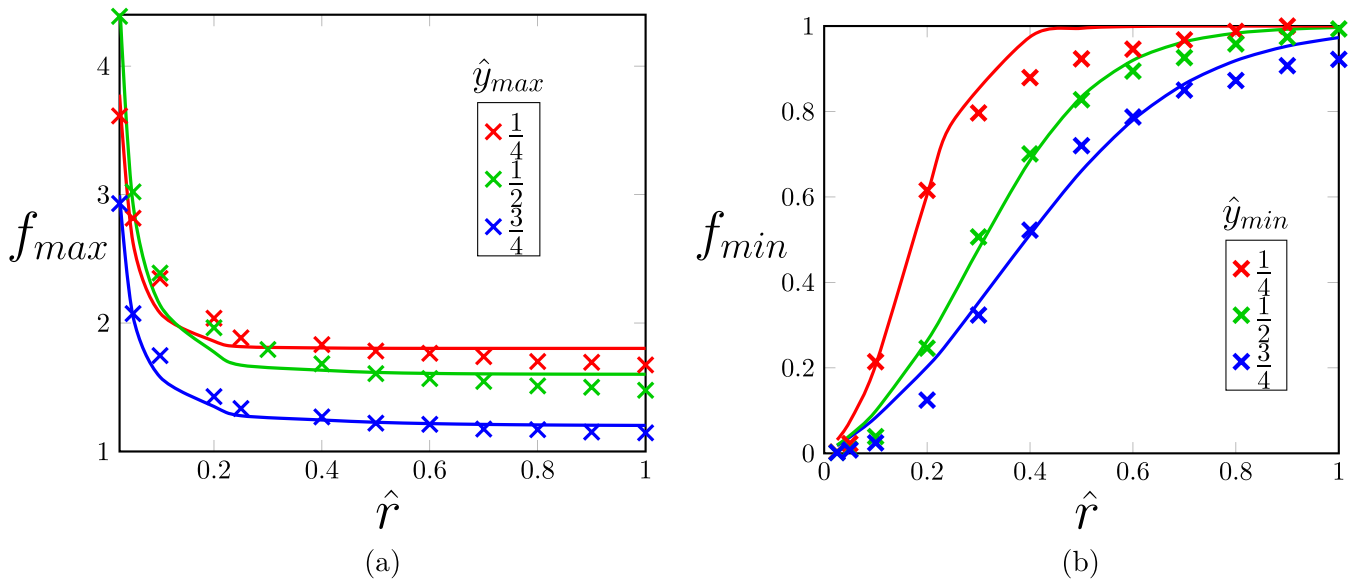


FIG. 7. (a) The augmentation coefficient  $f_{\max}$ ; (b) the diminishing coefficient  $f_{\min}$  versus normalized curvature of the interface  $\hat{r}$  for three quartile stages of the interface growth as  $\hat{y}_I := \{1/8, 2/8, 3/8\}$ . (a) Tracking the variation of the augmentation ratio  $f_{\max}$  with respect to the radius of curvature  $\hat{r}$  in the convex interface for various interface height  $\hat{y}_{\max}$ .  $\times$ : numerical computations, solid: interpolation via Eq. (24). (b) Tracking the variation of diminishing ratio  $f_{\min}$  with respect to the radius of curvature  $\hat{r}$  in the concave interface for various average interface height  $\hat{y}_{\min}$ .  $\times$ : numerical computations, solid: interpolation via Eq. (25).



various the normalized elevation of the growing interface  $\hat{y}_l = \{1/8, 1/4, 3/8\}$ , which is derived both from the numerical computations and interpolating functions [85]. As expected, their highest difference occurs when the radius of curvature turns extremely small into the atomic scale ( $\hat{r} \rightarrow r_{\text{atom}}/h \approx 0$ ), whereas they both converge to unity as the radius of curvature grows indefinitely large ( $\hat{r} \rightarrow \infty$ ) and the interface merges into a flat surface.

Finally, since considering mechanics as an additional factor has been expressed in terms of the localized surface tension altering the electrochemical potential [64,87], herein we explore the role of imposing global compressive external stress  $\sigma_0$  (or formation of internal global misfit stress) from a physical perspective. A simple approach would be to explore the role of the strength of the interface medium in altering the ratio of the electrodeposition rate in the peaks ( $\neg$ ) versus the valleys ( $\smile$ ). In this regard, the stability factor  $\chi$  can be defined as

$$\chi = \frac{J_{0,\neg} + J_{\sigma,\neg}}{J_{0,\smile} + J_{\sigma,\smile}}, \quad (26)$$

where  $J_{0,\neg}$ ,  $J_{0,\smile}$  are the ionic flux in the absence of the external stress  $\sigma_0$  (prominent diffusion and electromigration terms) and  $J_{\sigma,\neg}$ ,  $J_{\sigma,\smile}$  are the current flux due to sole effect of stress  $\sigma_0$ . Thus,  $\chi \leq 1$  and  $\chi > 1$  infer stable and unstable interface growth regimes. Since the electrolytic medium is the route of the stress transfer from the external boundary to the zones of peaks and valley, herein we categorize the electrolytic medium into two extreme states of the liquid and solid phases. Regarding the solid electrolyte, the peak regions will have a smaller footprint (stress concentration) and the stress is augmented to  $f_{\text{max}}\sigma_0$ , whereas the valley regions are enclosed more and get assisted from their peripheral zones for bearing the applied load, hence the carried stress will get diminished to  $f_{\text{min}}\sigma_0$ ; not to mention that closer proximity of the peaks to the counter electrode means larger straining and stress during the elastic behavior. Therefore,  $J_{\sigma,\neg} > J_{\sigma,\smile}$ . However, for the case of liquid electrolytes, the applied external compressive load  $\sigma_0$  will equally be distributed in peaks and valley zones due to Pascal's law [88], therefore,  $J_{\sigma,\neg} \approx J_{\sigma,\smile}$  and perhaps for a

dense-enough electrolyte ( $\rho \uparrow$ ) and large-enough perturbation ( $A \uparrow$ ), the concave region carries slightly larger stress of  $2\rho gA$ . Ultimately, one can summarize the role of external (or internal misfit) pressure  $\sigma_0$  on the stability of the growing interface as the following, where  $E$ ,  $G$  are the elastic and shear moduli of the electrolyte, respectively:

Electrolyte	$E, G$	$\sigma_0$ effect	Flux ratio	Total effect
Solid	$\uparrow\uparrow$	$J_{\sigma,\neg} > J_{\sigma,\smile}$	$\chi \uparrow$	Less stable
Liquid	$\downarrow\downarrow$	$J_{\sigma,\neg} \approx J_{\sigma,\smile}$	$\chi \downarrow$	More stable

## V. CONCLUSION

In this paper, we have developed an analytical and computational framework on the roughened growing interface, which is destabilized by the electric field bias, favoring the peaks (i.e., convex) over the valleys (i.e., concave). Imposing a countering temperature field in the electrodes, we established a stability criterion for quantifying the space of required temperature gradient  $\Delta T$  versus the activation energy of diffusion  $Q$ , leading to the controlled interface growth. As well, we also formulated a curvature-dependent analytical approximation for augmentation and diminishing ratios for the electric field in the vicinity of the convex (concave) interface. Such criterion establishes a relationship between the geometry of the interface, the physical properties of the electrolyte, and the operating conditions. The developed framework could be useful for designing the space of operational parameters for controlling the propagation of the microstructures and the prevention of runaway, during prolonged cycles, particularly when the surface roughness gets pronounced in the later stages of cycle life.

## DATA AVAILABILITY

The data that support the findings of this article are not publicly available. The data are available from the authors upon reasonable request.

- [1] P. J. Hall and E. J. Bain, Energy-storage technologies and electricity generation, *Energy Policy* **36**, 4352 (2008).
- [2] Y. Wang, B. Liu, Q. Li, S. Cartmell, S. Ferrara, Z. D. Deng, and J. Xiao, Lithium and lithium ion batteries for applications in microelectronic devices: A review, *J. Power Sources* **286**, 330 (2015).
- [3] B. Kennedy, D. Patterson, and S. Camilleri, Use of lithium-ion batteries in electric vehicles, *J. Power Sources* **90**, 156 (2000).
- [4] M. S. Whittingham, History, evolution, and future status of energy storage, *Proc. IEEE* **100**, 1518 (2012), Special Centennial Issue.
- [5] P. Gu, M. Zheng, Q. Zhao, X. Xiao, H. Xue, and H. Pang, Rechargeable zinc-air batteries: A promising way to green energy, *J. Mater. Chem. A* **5**, 7651 (2017).
- [6] R. Van Noorden, The rechargeable revolution: A better battery, *Nature (London)* **507**, 26 (2014).
- [7] A. Innocenti, D. Bresser, J. Garche, and S. Passerini, A critical discussion of the current availability of lithium and zinc for use in batteries, *Nat. Commun.* **15**, 4068 (2024).
- [8] T. Kim, W. Song, D.-Y. Son, L. K. Ono, and Y. Qi, Lithium-ion batteries: outlook on present, future, and hybridized technologies, *J. Mater. Chem. A* **7**, 2942 (2019).
- [9] J. Deng, X. Yang, and G. Zhang, Simulation study on internal short circuit of lithium ion battery caused by lithium dendrite, *Mater. Today Commun.* **31**, 103570 (2022).
- [10] R. Wang, W. Cui, F. Chu, and F. Wu, Lithium metal anodes: Present and future, *J. Energy Chem.* **48**, 145 (2020).
- [11] G. Rong, X. Zhang, W. Zhao, Y. Qiu, M. Liu, F. Ye, Y. Xu, J. Chen, Y. Hou, W. Li *et al.*, Liquid-phase electrochemical scanning electron microscopy for in situ investigation of lithium dendrite growth and dissolution, *Adv. Mater.* **29**, 1606187 (2017).

- [12] K. Xu, Nonaqueous liquid electrolytes for lithium-based rechargeable batteries, *Chem. Rev.* **104**, 4303 (2004).
- [13] D. Tewari, S. P. Rangarajan, P. B. Balbuena, Y. Barsukov, and P. P. Mukherjee, Mesoscale anatomy of dead lithium formation, *J. Phys. Chem. C* **124**, 6502 (2020).
- [14] J. Wang, S. Yi, J. Liu, S. Sun, Y. Liu, D. Yang, K. Xi, G. Gao, A. Abdelkader, W. Yan *et al.*, Suppressing the shuttle effect and dendrite growth in lithium-sulfur batteries, *ACS Nano* **14**, 9819 (2020).
- [15] D. Lin, Y. Liu, and Y. Cui, Reviving the lithium metal anode for high-energy batteries, *Nat. Nanotechnol.* **12**, 194 (2017).
- [16] F. Orsini, A. D. Pasquier, B. Beaudoin, and J. M. Tarascon, In situ scanning electron microscopy (SEM) observation of interfaces with plastic lithium batteries, *J. Power Sources* **76**, 19 (1998).
- [17] C. Brissot, M. Rosso, J. N. Chazalviel, and S. Lascaud, Dendritic growth mechanisms in lithium/polymer cells, *J. Power Sources* **81-82**, 925 (1999).
- [18] H. Sano, H. Sakaebe, H. Senoh, and H. Matsumoto, Effect of current density on morphology of lithium electrodeposited in ionic liquid-based electrolytes, *J. Electrochem. Soc.* **161**, A1236 (2014).
- [19] O. Crowther and A. C. West, Effect of electrolyte composition on lithium dendrite growth, *J. Electrochem. Soc.* **155**, A806 (2008).
- [20] N. Schweikert, A. Hofmann, M. Schulz, M. Scheuermann, S. T. Boles, T. Hanemann, H. Hahn, and S. Indris, Suppressed lithium dendrite growth in lithium batteries using ionic liquid electrolytes: Investigation by electrochemical impedance spectroscopy, scanning electron microscopy, and *in situ* Li-7 nuclear magnetic resonance spectroscopy, *J. Power Sources* **228**, 237 (2013).
- [21] H. Liu, X.-B. Cheng, J.-Q. Huang, H. Yuan, Y. Lu, C. Yan, G.-L. Zhu, R. Xu, C.-Z. Zhao, L.-P. Hou *et al.*, Controlling dendrite growth in solid-state electrolytes, *ACS Energy Lett.* **5**, 833 (2020).
- [22] N. Takenaka, A. Bouibes, Y. Yamada, M. Nagaoka, and A. Yamada, Frontiers in theoretical analysis of solid electrolyte interphase formation mechanism, *Adv. Mater.* **33**, 2100574 (2021).
- [23] J. Steiger, D. Kramer, and R. Monig, Mechanisms of dendritic growth investigated by *in situ* light microscopy during electrodeposition and dissolution of lithium, *J. Power Sources* **261**, 112 (2014).
- [24] K. Rafiz, D. R. Lingam Murali, and J. Y. S. Lin, Suppressing lithium dendrite growth on lithium-ion/metal batteries by a tortuously porous  $\gamma$ -alumina separator, *Electrochim. Acta* **421**, 140478 (2022).
- [25] I. V. Thorat, D. E. Stephenson, N. A. Zacharias, K. Zaghib, J. N. Harb, and D. R. Wheeler, Quantifying tortuosity in porous li-ion battery materials, *J. Power Sources* **188**, 592 (2009).
- [26] A. Cannon and E. M. Ryan, Characterizing the microstructure of separators in lithium batteries and their effects on dendritic growth, *ACS Appl. Energy Mater.* **4**, 7848 (2021).
- [27] C. P. Nielsen and H. Bruus, Morphological instability during steady electrodeposition at overlimiting currents, *Phys. Rev. E* **92**, 052310 (2015).
- [28] A. Aryanfar, A. Tayyar, and W. A. Goddard III, Dendritic propagation on circular electrodes: The impact of curvature on the packing density, *Phys. Rev. E* **108**, 014801 (2023).
- [29] P. Bai, J. Li, F. R. Brushett, and M. Z. Bazant, Transition of lithium growth mechanisms in liquid electrolytes, *Energy Environ. Sci.* **9**, 3221 (2016).
- [30] P. P. Natsiavas, K. Weinberg, D. Rosato, and M. Ortiz, Effect of prestress on the stability of electrode-electrolyte interfaces during charging in lithium batteries, *J. Mech. Phys. Solids* **95**, 92 (2016).
- [31] S. Wei, Z. Cheng, P. Nath, M. D. Tikekar, G. Li, and L. A. Archer, Stabilizing electrochemical interfaces in viscoelastic liquid electrolytes, *Sci. Adv.* **4**, eaao6243 (2018).
- [32] I. Rubinstein and B. Zaltzman, Electro-osmotically induced convection at a permselective membrane, *Phys. Rev. E* **62**, 2238 (2000).
- [33] G. Liu and W. Lu, A model of concurrent lithium dendrite growth, SEI growth, SEI penetration and regrowth, *J. Electrochem. Soc.* **164**, A1826 (2017).
- [34] W. Liu, P. Liu, and D. Mitlin, Review of emerging concepts in SEI analysis and artificial SEI membranes for lithium, sodium, and potassium metal battery anodes, *Adv. Energy Mater.* **10**, 2002297 (2020).
- [35] Z. Jiang, M. Pang, C. Luo, Z. Yao, T. Fu, T. Pan, W. Sun, Y. Li, Q. Guo, S. Xiong *et al.*, Curvature-induced strain to realize differential lithiophilicity for selective lithium deposition and stable lithium anode, *Energy Storage Mater.* **72**, 103729 (2024).
- [36] O. Borodin, X. Ren, J. Vatamanu, A. von Wald Cresce, J. Knap, and K. Xu, Modeling insight into battery electrolyte electrochemical stability and interfacial structure, *Acc. Chem. Res.* **50**, 2886 (2017).
- [37] J. Choi, D. Crowdy, and M. Z. Bazant, Diffusion-limited aggregation on curved surfaces, *Europhys. Lett.* **91**, 46005 (2010).
- [38] D. A. Cogswell, Quantitative phase-field modeling of dendritic electrodeposition, *Phys. Rev. E* **92**, 011301(R) (2015).
- [39] C.-H. Chen and C.-W. Pao, Phase-field study of dendritic morphology in lithium metal batteries, *J. Power Sources* **484**, 229203 (2021).
- [40] A. Jana, D. R. Ely, and R. E. García, Dendrite-separator interactions in lithium-based batteries, *J. Power Sources* **275**, 912 (2015).
- [41] A. Aryanfar, D. Brooks, B. V. Merinov, W. A. Goddard III, A. J. Colussi, and M. R. Hoffmann, Dynamics of lithium dendrite growth and inhibition: Pulse charging experiments and Monte Carlo calculations, *J. Phys. Chem. Lett.* **5**, 1721 (2014).
- [42] C. P. Nielsen and H. Bruus, Sharp-interface model of electrodeposition and ramified growth, *Phys. Rev. E* **92**, 042302 (2015).
- [43] T. Foroozan, F. A. Soto, V. Yurkiv, S. Sharifi-Asl, R. Deivanayagam, Z. Huang, R. Rojaee, F. Mashayek, P. B. Balbuena, and R. Shahbazian-Yassar, Synergistic effect of graphene oxide for impeding the dendritic plating of Li, *Adv. Funct. Mater.* **28**, 1705917 (2018).
- [44] J. L. Andrews, P. Stein, D. A. Santos, C. J. Chalker, L. R. De Jesus, R. D. Davidson, M. A. Gross, M. Pharr, J. D. Batteas, B.-X. Xu *et al.*, Curvature-induced modification of mechano-electrochemical coupling and nucleation kinetics in a cathode material, *Matter* **3**, 1754 (2020).
- [45] L. Cao, D. Liu, P. Jiang, X. Shao, Q. Zhou, and Y. Wang, Multi-physics simulation of dendritic growth in magnetic field assisted solidification, *Int. J. Heat Mass Transf.* **144**, 118673 (2019).
- [46] D. Cipollone, H. Yang, F. Yang, J. Bright, B. Liu, N. Winch, N. Wu, and K. A. Sierros, 3d printing of an anode scaffold

- for lithium batteries guided by mixture design-based sequential learning, *J. Mater. Process. Technol.* **295**, 117159 (2021).
- [47] L. Shi, L. Zhang, Y. Yang, H. Zhang, R. Yao, C. Yuan, and S. Cheng, In situ nano-sio<sub>2</sub> electrospun polyethylene-oxide-based nano-fiber composite solid polymer electrolyte for high-performance lithium-ion batteries, *Nanomaterials* **13**, 1294 (2023).
- [48] W. Li, H. A. Tchelepi, Y. Ju, and D. M. Tartakovsky, Stability-guided strategies to mitigate dendritic growth in lithium-metal batteries, *J. Electrochem. Soc.* **169**, 060536 (2022).
- [49] R. Akolkar, Mathematical model of the dendritic growth during lithium electrodeposition, *J. Power Sources* **232**, 23 (2013).
- [50] M. N. Parekh, C. D. Rahn, and L. A. Archer, Controlling dendrite growth in lithium metal batteries through forced advection, *J. Power Sources* **452**, 227760 (2020).
- [51] M. C. Ma, G. Li, X. Chen, L. A. Archer, and J. Wan, Suppression of dendrite growth by cross-flow in microfluidics, *Sci. Adv.* **7**, eabf6941 (2021).
- [52] L. T. Gao and Z.-S. Guo, Effects of optimized electrode surface roughness and solid electrolyte interphase on lithium dendrite growth, *Energy Tech.* **9**, 2000968 (2021).
- [53] H. Lee, T. Kwak, W. Lee, J. Song, and D. Kim, Effect of surface topography on dendritic growth in lithium metal batteries, *J. Power Sources* **552**, 232264 (2022).
- [54] H. Liu, X.-B. Cheng, Z. Jin, R. Zhang, G. Wang, L.-Q. Chen, Q.-B. Liu, J.-Q. Huang, and Q. Zhang, Recent advances in understanding dendrite growth on alkali metal anodes, *EnergyChem* **1**, 100003 (2019).
- [55] M. Armand, Polymer solid electrolytes-an overview, *Solid State Ionics* **9-10**, 745 (1983).
- [56] D. Wheeler, D. Josell, and T. P. Moffat, Modeling super-conformal electrodeposition using the level set method, *J. Electrochem. Soc.* **150**, C302 (2003).
- [57] T. P. Moffat, D. Wheeler, S.-K. Kim, and D. Josell, Curvature enhanced adsorbate coverage model for electrodeposition, *J. Electrochem. Soc.* **153**, C127 (2006).
- [58] N. Sezer and M. Koç, A comprehensive review on the state-of-the-art of piezoelectric energy harvesting, *Nano Energy* **80**, 105567 (2021).
- [59] H. Liu, J. Zhong, C. Lee, S.-W. Lee, and L. Lin, A comprehensive review on piezoelectric energy harvesting technology: Materials, mechanisms, and applications, *Appl. Phys. Rev.* **5**, 041306 (2018).
- [60] W. W. Mullins and R. F. Sekerka, Morphological stability of a particle growing by diffusion or heat flow, *J. Appl. Phys.* **34**, 323 (1963).
- [61] J. L. Barton and J. O'M Bockris, The electrolytic growth of dendrites from ionic solutions, *Proc. R. Soc. London A* **268**, 485 (1962).
- [62] A. Verma, H. Kawakami, H. Wada, A. Hirowatari, N. Ikeda, Y. Mizuno, T. Kotaka, K. Aotani, Y. Tabuchi, and P. P. Mukherjee, Microstructure and pressure-driven electrodeposition stability in solid-state batteries, *Cell Rep. Phys. Sci.* **2**, 100301 (2021).
- [63] C. Yuan, W. Lu, and J. Xu, Unlocking the electrochemical-mechanical coupling behaviors of dendrite growth and crack propagation in all-solid-state batteries, *Adv. Energy Mater.* **11**, 2101807 (2021).
- [64] C. Monroe and J. Newman, The effect of interfacial deformation on electrodeposition kinetics, *J. Electrochem. Soc.* **151**, A880 (2004).
- [65] A. N. Dey, Lithium anode film and organic and inorganic electrolyte batteries, *Thin Solid Films* **43**, 131 (1977).
- [66] H. Ota, X. Wang, and E. Yasukawa, Characterization of lithium electrode in lithium imides/ethylene carbonate, and cyclic ether electrolytes: I. Surface morphology and lithium cycling efficiency, *J. Electrochem. Soc.* **151**, A427 (2004).
- [67] R. Mogi, M. Inaba, Y. Iriyama, T. Abe, and Z. Ogumi, In situ atomic force microscopy study on lithium deposition on nickel substrates at elevated temperatures, *J. Electrochem. Soc.* **149**, A385 (2002).
- [68] A. Aryanfar, D. J. Brooks, A. J. Colussi, B. V. Merinov, W. A. Goddard III, and M. R. Hoffmann, Thermal relaxation of lithium dendrites, *Phys. Chem. Chem. Phys.* **17**, 8000 (2015).
- [69] A. Aryanfar, T. Cheng, A. J. Colussi, B. V. Merinov, W. A. Goddard III, and M. R. Hoffmann, Annealing kinetics of electrodeposited lithium dendrites, *J. Chem. Phys.* **143**, 134701 (2015).
- [70] A. Maraschky and R. Akolkar, Temperature dependence of dendritic lithium electrodeposition: a mechanistic study of the role of transport limitations within the SEI, *J. Electrochem. Soc.* **167**, 062503 (2020).
- [71] H. H. Yan, Y. H. Bie, X. Y. Cui, G. P. Xiong, and L. Chen, A computational investigation of thermal effect on lithium dendrite growth, *Energy Convers. Manage.* **161**, 193 (2018).
- [72] R. Akolkar, Modeling dendrite growth during lithium electrodeposition at sub-ambient temperature, *J. Power Sources* **246**, 84 (2014).
- [73] C. T. Love, O. A. Baturina, and K. E. Swider-Lyons, Observation of lithium dendrites at ambient temperature and below, *ECS Electrochem. Lett.* **4**, A24 (2015).
- [74] A. Aryanfar, S. Medlej, and W. A. Goddard III, Morphometry of dendritic materials in rechargeable batteries, *J. Power Sources* **481**, 228914 (2021).
- [75] K. J. Laidler, The development of the Arrhenius equation, *J. Chem. Educ.* **61**, 494 (1984).
- [76] A. J. Bard, R. Parsons, and J. Jordan, *Standard Potentials in Aqueous Solution*, International Union of Pure and Applied Chemistry (Marcel Dekker Inc., New York, NY, 1985), Vol. 6.
- [77] R. A. Naulty and D. G. Leaist, Diffusion in aqueous copper sulfate and copper sulfate-sulfuric acid solutions, *J. Solution Chem.* **16**, 813 (1987).
- [78] J. Ahn, M. Kim, J. Seo, S. Yoon, and K. Y. Cho, Delineating the relationship between separator parameters and practical lithium metal batteries characteristics, *J. Power Sources* **566**, 232931 (2023).
- [79] Standard, Data Encryption, Federal Information Processing Standard (FIPS) Publication Vol. 46 (National Institute of Standards and Technology, Gaithersburg, MD, 2002), p. 20899.
- [80] J.-L. Shi, D.-D. Xiao, M. Ge, X. Yu, Y. Chu, X. Huang, X.-D. Zhang, Y.-X. Yin, X.-Q. Yang, Y.-G. Guo *et al.*, High-capacity cathode material with high voltage for Li-ion batteries, *Adv. Mater.* **30**, 1705575 (2018).
- [81] A. J. Bard and L. R. Faulkner, *Electrochemical Methods: Fundamentals and Applications*, 2nd ed. (Wiley, New York, 1980).
- [82] J. N. Chazalviel, Electrochemical aspects of the generation of ramified metallic electrodeposits, *Phys. Rev. A* **42**, 7355 (1990).
- [83] D. J. Griffiths, *Introduction to Electrodynamics* (Cambridge University Press, Cambridge, UK, 2023).

- [84] R. F. Probstein, *Physicochemical Hydrodynamics: An Introduction* (John Wiley & Sons, New York, NY, 2005).
- [85] See Supplemental Material at <http://link.aps.org/supplemental/10.1103/PhysRevE.111.015505> for computing the following: (1) the convergence on the spatial distribution, the maximum and the minimum values of the electric field; (2) computing the stable zone in the space of temperature gradient versus activation energy for diffusivity of the electrolyte; and (3) computing the curvature-induced augmentation and diminishing ratios for the electric field and the subsequent nonlinear interpolation.
- [86] T. L. Bergman, T. L. Bergman, F. P. Incropera, D. P. Dewitt, and A. S. Lavine, *Fundamentals of Heat and Mass Transfer* (John Wiley & Sons, Danvers, MA, 2011).
- [87] Z. Ahmad and V. Viswanathan, Stability of electrodeposition at solid-solid interfaces and implications for metal anodes, *Phys. Rev. Lett.* **119**, 056003 (2017).
- [88] D. H. A. L. Anselmo, J. M. Hidalgo, and D. M. Queiroz, Pascals principle revisited a critical review of physics undergraduate textbooks, *Eur. J. Phys.* **41**, 063001 (2020).